Nonempirical hybrid functionals for band gaps of inorganic metal-halide perovskites

Nonempirical hybrid functionals for band gaps of inorganic metal-halide perovskites

Thomas Bischoff,[1,*] Julia Wiktor,[1,2] Wei Chen,[3] and Alfredo Pasquarello[1]

[1]*Chaire de Simulation à l' Echelle Atomique (CSEA), Ecole Polytechnique Fédérale de Lausanne (EPFL),CH-1015 Lausanne, Switzerland*

[2]*Department of Physics, Chalmers University of Technology, SE-412 96 Gothenburg, Sweden*

[3]*Institute of Condensed Matter and Nanoscience (IMCN), Université catholique de Louvain, B-1348 Louvain-la-Neuve, Belgium*

(Received 4 October 2019; published 16 December 2019)

Nonempirical hybrid functionals are investigated for band-gap predictions of inorganic metal-halide perovskites belonging to the class CsBX_3, with B = Ge, Sn, Pb and X = Cl, Br, I. We consider both global and range-separated hybrid functionals and determine the parameters through two different schemes. The first scheme is based on the static screening response of the material and thus yields dielectric-dependent hybrid functionals. The second scheme defines the hybrid functionals through the enforcement of Koopmans' condition for localized defect states. We also carry out quasiparticle self-consistent *GW* calculations with vertex corrections to establish state-of-the-art references. For the investigated class of materials, dielectric-dependent functionals and those fulfilling Koopmans' condition yield band gaps of comparable accuracy (∼0.2 eV), but the former only require calculations for the primitive unit cell and are less subject to the specifics of the material.

DOI: 10.1103/PhysRevMaterials.3.123802

I. INTRODUCTION

Solar cells based on metal-halide perovskites have recently drawn great scientific attention [1–5]. In fact, within one decade their power conversion efficiencies increased tremendously [1,3] and reached 22.1% in 2017 [5] with potential for improving even further. This makes them stand out as a promising alternative to today's best thin-film photovoltaic devices [2,4]. The further improvement of perovskite solar cells relies greatly on the ability of exploring the immense space of possible compositions and structures. For this task, one naturally resorts to automated computational methods [6–8]. This requires a critical trade off between aspired accuracy and bearable effort. The most accurate technique for band-gap evaluation consists of quasiparticle self-consistent *GW* calculations including vertex corrections [9–12]. However, this technique demands a high computational effort and is practically limited to materials with small unit cells. In particular, a recent study on perovskite compounds accounting for spin-orbit and thermal effects showed that this level of theory is needed to achieve a good comparison with experimental band gaps [13]. Therefore it is highly desirable to develop alternative computational schemes yielding the same accuracy as self-consistent *GW* methods but requiring a lower computational cost.

Electronic-structure calculations based on hybrid functionals [14–17] have the potential to fill this gap. Such functionals show an improved description of the electronic structure [18] compared to standard density functionals in semilocal approximations [19–21]. However, hybrid functionals remain unsatisfactory because they contain undetermined parameters, such as the amount of incorporated Fock exchange. To overcome this deficiency, two different nonempirical determination schemes are being investigated at present, namely, dielectric-dependent hybrid (DDH) functionals [22–32] and hybrid functionals enforcing Koopmans' condition [33–40]. Both approaches exhibit great potential due to their promising combination of accuracy and computational cost. However, a comparative study of these techniques has so far only been reported for alkali-halide compounds [36].

In this work, we set out to evaluate the performance of various nonempirical hybrid functionals for inorganic metal-halide perovskites. We consider the cubic phase of CsBX_3 perovskites, where B represents Ge, Sn, or Pb and X stands for Cl, Br, or I. These compounds serve as a representative set of metal-halide perovskites and additionally show sufficiently small unit cells to make high-level reference calculations affordable. The parameters in the hybrid functionals constructed here are determined both through the static dielectric response and through the enforcement of Koopmans' condition. Our work carefully goes through the construction process highlighting all critical issues encountered, thereby allowing clear insight into the viability of the two approaches. To achieve reference band gaps, we additionally perform state-of-the-art *GW* calculations within a consistent computational setup. The present analysis allows us to determine the accuracy of the investigated schemes in a comparative fashion and to discuss their suitability for application to the screening of large sets of perovskite materials.

This work is organized as follows. We first introduce the considered theoretical schemes in Sec. II. We then provide computational details in Sec. III and highlight the role of exchange interactions with semicore electrons. In Sec. IV, we show band gaps obtained with the constructed hybrid functionals. We draw conclusions in Sec. V.

II. THEORETICAL SCHEMES

In this work, we apply nonempirical construction schemes to different classes of hybrid functionals. In particular, we consider global as well as range-separated hybrid density

*thomas.bischoff@epfl.ch

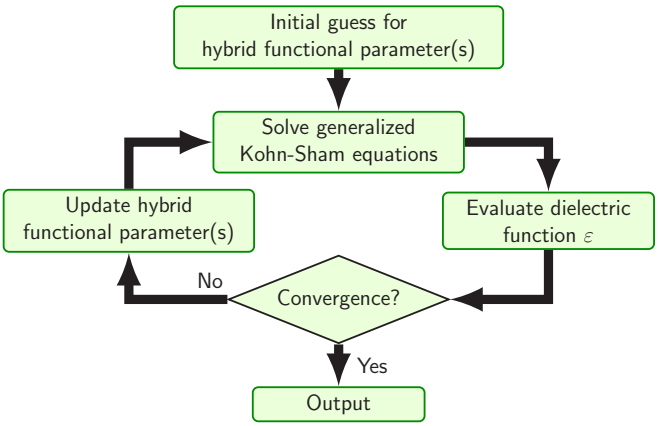

FIG. 1. Workflow for the construction of dielectric-dependent hybrid (DDH) functionals. The procedure for updating the free parameters depends on the considered hybrid-functional form and is described in the text.

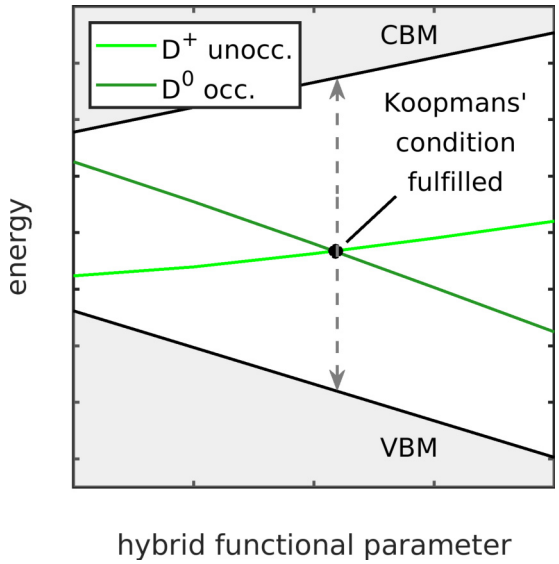

FIG. 2. Scheme for the construction of a hybrid functional satisfying Koopmans' condition through a defect D. Occupied and unoccupied single-particle energy levels are given as a function of the free parameter of the adopted hybrid functional form. The point of intersection corresponds to the fulfillment of Koopmans' condition. The band edges of the host material are also shown as a function of the hybrid functional parameter. The dashed vertical line represents the resulting band-gap estimate.

functionals and determine their free parameters. For the former, we use the functional PBE0(α), which depends only on the incorporated fraction of Fock exchange α [15]. For the latter, we consider range-separated hybrid functionals based on the Coulomb-attenuating method (CAM) of Yanai *et al.* [17]. This functional incorporates different fractions of Fock exchange in the short (α_s) and in the long range (α_ℓ), mediated via the inverse screening length μ.

A. Dielectric-dependent hybrid functionals

The concept of DDH functionals consists in determining the free parameters of a hybrid functional via the dielectric response of the considered material. The connection between these quantities was first observed for the fraction of Fock exchange α and the inverse macroscopic dielectric constant $1/\varepsilon_\infty$ [18,25]. Various authors contributed to the further development of this basic idea, in particular through the use of self-consistent update schemes [23,27,28] and the extension to range-separated hybrid functionals [30,32]. In particular, in Ref. [32], all the parameters of the DDH functional are extracted from the static dielectric response function.

In this study, we determine DDH functionals following the procedure outlined in Ref. [32]. The workflow of this procedure is visualized in Fig. 1. It consists of an iterated update of an initial guess for the hybrid functional parameters. Within each iteration step, the generalized Kohn-Sham equations [41] are solved and the dielectric function ε of the considered material is calculated. Subsequently, improved values of the hybrid functional parameters are determined using the calculated dielectric properties. This process is performed until a self-consistent description of the free parameters and ε is reached.

We remark that the update step in Fig. 1 depends on the adopted family of hybrid functionals. For the global functional PBE0(α), the mixing parameter α is updated in the standard fashion via the inverse high-frequency dielectric constant: $\alpha = 1/\varepsilon_\infty$. For the case of the range-separated functional CAM($\alpha_s, \alpha_\ell, \mu$), α_s is set to 1, $\alpha_\ell = 1/\varepsilon_\infty$, and μ is determined through a fitting procedure [32]. This is equivalent to the enforcement of a model dielectric function, which can be expressed in reciprocal space as

$$\varepsilon^{-1}(G) = 1 - \left(1 - \varepsilon_\infty^{-1}\right) e^{-G^2/4\mu^2}. \quad (1)$$

For the nonempirical hybrid functionals determined in this way, we here use the notation DD-PBE0 and DD-CAM.

B. Hybrid functionals satisfying Koopmans' condition

The second construction scheme for nonempirical hybrid functionals considered in this work is based on the enforcement of Koopmans' condition. This physical constraint states that for the exact density functional a single-particle level does not change upon its occupation [42]. Deviations from the Koopmans' condition within approximate density functional schemes have been associated with the many-body self-interaction error [43,44].

For the construction of a hybrid functional that satisfies Koopmans' condition, we use the procedure shown in Fig. 2 [36,39]. We study single-particle energy levels induced by point defects within a supercell of the considered material. We perform hybrid functional calculations in two charge configurations, in which the localized state is either occupied or unoccupied. The single-particle levels observed in the two configurations evolve depending on the free parameter and their point of intersection indicates the fulfillment of Koopmans' condition. The use of two extreme cases of occupation minimizes the numerical errors associated with the determination of the intersection. The hybrid functional defined by the corresponding parameter is then used to obtain an estimate of the band gap of the host material. In analogy to the case of DDH functionals, we use the notation K-PBE0 and K-CAM

TABLE I. Construction schemes investigated in this work. We consider global hybrid functionals with a single undetermined parameter (PBE0) and range-separated hybrid functionals involving three parameters (CAM). The parameters are determined either through the static dielectric response or through the enforcement of Koopmans' condition.

	Global	Range-separated
Dielectric dependent	DD-PBE0	DD-CAM
Koopmans' condition	K-PBE0	K-CAM

for the nonempirical hybrid functionals determined via this scheme. Table I summarizes the various schemes investigated in this work.

C. Quasiparticle self-consistent *GW* with vertex corrections as reference method

To evaluate the performance of nonempirical hybrid functionals, we carry out comparisons with state-of-the-art methods for band-gap evaluation. Quasiparticle self-consistent *GW* (QS$G\tilde{W}$) including vertex corrections in the screening ($\tilde{W}$) can serve as such a high-level reference [9–12]. A detailed QS$G\tilde{W}$ study of inorganic metal-halide perovskites has recently been carried out by Wiktor *et al.* [13]. Here, we calculate QS$G\tilde{W}$ band gaps in a similar fashion but with the pseudopotentials considered in this work and with nonlocal commutators for the optical matrix element in the long-wavelength limit as in Ref. [45]. Our QS$G\tilde{W}$ band gaps are given in Table II. In comparison to the results in Ref. [13], the present band gaps agree within ∼0.2 eV on average and thereby confirm the conclusions drawn previously.

The comparison with experiment requires the consideration of thermal effects and spin-orbit coupling [13]. For the Pb and Sn based perovskites, this can be achieved by relying on the corrections given in Ref. [13]. The calculated band gaps corrected in this way are compared with experimental band gaps in Table II. We generally consider experimental data for the same cubic phase when available, but report values referring to other phases otherwise. We observe that the QS$G\tilde{W}$ band gaps generally agree well with experiment after the consideration of thermal effects and spin-orbit coupling [13]. The case of $CsSnCl_3$ shows a deviation of about 0.6 eV, but this could at least partially result from the consideration of a cubic phase in the calculation and of a monoclinic one in the experiment. In the following, we do not refer to experimental data any more and use our QS$G\tilde{W}$ results to benchmark the band gaps obtained through the nonempirical hybrid-functional schemes.

TABLE II. Band gaps (in eV) as calculated through QS$G\tilde{W}$. Following Ref. [13], we include corrections for finite temperature effects (Δ_T) and for spin-orbit coupling (Δ_{SOC}) before comparing with experimental band gaps.

	QS$G\tilde{W}$	QS$G\tilde{W}$+Δ_T+Δ_{SOC}	Expt.
$CsPbI_3$	2.27	1.79	1.67 [49], 1.73 [50]
$CsPbBr_3$	3.01	2.24	2.25 [51], 2.36 [52]
$CsPbCl_3$	3.41	2.70	2.85 [51]
$CsSnI_3$	1.10	1.46	1.31[a] [53], 1.3[a] [54]
$CsSnBr_3$	1.32	1.75	1.75 [53]
$CsSnCl_3$	1.79	2.17	2.8[b] [53]
$CsGeI_3$	1.67	-	1.6[b] [55], 1.63[c] [56]
$CsGeBr_3$	2.13	-	2.38[d] [57]
$CsGeCl_3$	2.67	-	3.43[d] [57]

[a]Orthorhombic phase.
[b]Monoclinic phase.
[c]Trigonal phase.
[d]Rhombohedral phase.

The QS$G\tilde{W}$ calculations in this work are performed with computational parameters consistent with Ref. [13]. In particular, we used a $4 \times 4 \times 4$ **k**-point sampling and a plane-wave cutoff of 100 Ry. We include 800 bands and achieve results in the infinite basis-set limit through linear extrapolation with respect to the inverse number of bands [46]. For the materials investigated here, we find that such an extrapolation generally leads to a band-gap opening of ∼0.1 eV. In particular, we only update the lowest 80 bands self-consistently and keep those obtained with the semilocal Perdew-Burke-Ernzerhof (PBE) functional for the higher-lying states [21]. We verify that the update of more bands does not lead to a discernible change in the band gap. The frequency dependence of the dielectric function is evaluated through the contour deformation technique [47]. We take into account eight real and four imaginary frequencies, and use a plane-wave cutoff of 16 Ry for the dielectric function. The vertex corrections are included as in Ref. [12]. We verify that the adopted parameters ensure the convergence of the quasiparticle energy levels within 0.05 eV. The QS$G\tilde{W}$ calculations are performed with the code ABINIT [48].

III. COMPUTATIONAL METHODS

A. Computational details

The calculations presented in this work are carried out using experimental lattice constants of the cubic phase for the nine perovskites as given in Refs. [13,58]. We use two sets of normconserving pseudopotentials [59,60] to examine the role of exchange interactions with core states [61] (see Sec. III B). The first set (denoted PP1) incorporates only the outermost shells among the valence states, whereas the second set (denoted PP2) additionally includes semicore shells. The pseudopotential of Cs includes the semicore states in both sets. The reference *GW* calculations have been performed with the set PP2. We used cutoffs of 70 and 100 Ry for the sets PP1 and PP2, respectively. The valence electrons for all the elements in the pseudopotential sets are specified in Table III.

For the construction of DDH functionals, it is sufficient to address the primitive unit cells. Converged results for the band gap are achieved using a $4 \times 4 \times 4$ **k**-point sampling. For the proper evaluation of the high-frequency dielectric constants denser grids of $8 \times 8 \times 8$ for the Pb compounds and of $10 \times 10 \times 10$ for the Sn and Ge compounds are used. The Gygi-Baldereschi technique is used for treating the Coulomb singularity of the exchange potential [62,63]. The dielectric function is calculated through a linear response approach. The irreducible polarization is evaluated with the formula of Adler

TABLE III. Atomic shells treated among the valence electrons in the two different sets of pseudopotentials considered in this work.

	PP1	PP2
Cs	$5s^2 5p^6 6s^1$	$5s^2 5p^6 6s^1$
Ge	$3d^{10} 4s^2 4p^2$	$3s^2 3p^6 3d^{10} 4s^2 4p^2$
Sn	$4d^{10} 5s^2 5p^2$	$4s^2 4p^6 4d^{10} 5s^2 5p^2$
Pb	$5d^{10} 6s^2 6p^2$	$5s^2 5p^6 5d^{10} 6s^2 6p^2$
Cl	$3s^2 3p^5$	$2s^2 2p^6 3s^2 3p^5$
Br	$4s^2 4p^5$	$3s^2 3p^6 3d^{10} 4s^2 4p^5$
I	$5s^2 5p^5$	$4s^2 4p^6 4d^{10} 5s^2 5p^5$

and Wiser [64,65], for which 500 bands and an energy cutoff of 16 Ry are found to give converged results. For a more realistic description, we calculate the reducible polarizability including the bootstrap exchange-correlation kernel [66] for treating vertex corrections [32]. The calculations for the DDH functionals are carried out with ABINIT [48].

The construction of hybrid functionals satisfying Koopmans' condition is based on calculations for defects in supercells [36]. For modeling the point defects, we use $2 \times 2 \times 2$ supercells (40 atoms) together with $2 \times 2 \times 2$ **k**-point samplings. Spin polarization is explicitly included whenever unpaired electrons occur. Upon the creation of the defect, the electronic structure is calculated fully self-consistently without allowing for structural relaxation. Therefore the long-range screening is described entirely by the high-frequency dielectric constant ε_∞. The spurious interactions with image charges arising from the periodic boundary conditions are overcome through state-of-the-art finite-size corrections to the single-particle energy levels [67]. These corrections are systematically performed with dielectric constants that are consistent with the hybrid functionals used in the electronic-structure calculations. The calculations for the hybrid functionals satisfying Koopmans' condition are performed with QUANTUM ESPRESSO [68]. We use the same pseudopotentials [60] as in the calculations performed with ABINIT to ensure a meaningful comparison between the results of the two codes.

B. Role of semicore electrons

Preliminary to the construction of the nonempirical hybrid functionals, we devote special attention to the effect of including semicore shells among the valence electrons. To ensure consistency with the *GW* reference, the same PP2 pseudopotentials should be used in the hybrid functional calculations. This can be achieved with the DDH construction scheme, which relies on calculations in the primitive unit cell. However, the PP2 set of pseudopotentials becomes prohibitively demanding when dealing with defects in supercells. For the construction of hybrid functionals satisfying Koopmans' condition, we therefore make use of the lighter pseudopotentials in the set PP1.

In order to estimate the error that we introduce through neglecting the semicore electrons in PP1, we perform band-gap calculations using the two sets of pseudopotentials. In particular, we systematically vary the free parameters α_s and μ within the hybrid functional CAM(α_s, $\alpha_\ell = 1/\varepsilon_\infty$, μ). The form of the functional PBE0(α) is recovered by setting $\alpha = \alpha_s$ and $\mu \to 0$. The band-gap differences originating from the different pseudopotentials are visualized in Fig. 3 in the representative case of $CsPbI_3$. The two sets of pseudopotentials yield almost identical band gaps in the limit corresponding to the semilocal functional PBE ($\alpha_s = 0$ and $\mu = 0$). This is consistent with the fact that the two sets of pseudopotentials are generated at the PBE level and indicates that semicore states play a negligible role at this level of theory. When the fraction of Fock exchange incorporated in the functional is increased, we find that the PP1 set yields a reduction of the band gap with respect to the PP2 set. For low values of α_s, the difference in the band gap amounts to only a few tenths of an electronvolt, but it progressively increases with α_s, and reaches values larger than 1 eV for α_s approaching 1. This dependence indicates that the implicit treatment of semicore states in PP1 leads to significant discrepancies with respect to the more accurate PP2 set when the fraction of Fock exchange incorporated in the functional becomes sizable. Similar effects were observed by Stroppa *et al.* [61] for hybrid functional calculations with pseudopotentials generated at the semilocal level.

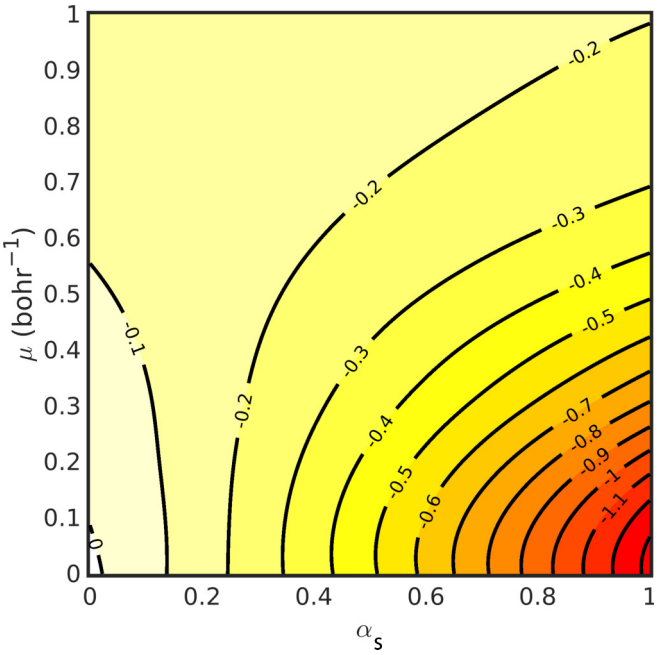

FIG. 3. Band-gap difference (in eV) for $CsPbI_3$ between calculations with pseudopotential sets PP1 and PP2, which differ by the treatment of semicore electrons. The band gaps are obtained with a CAM-type hybrid functional in which the long-range fraction of Fock exchange is set to $\alpha_\ell = 1/\varepsilon_\infty$. The figure shows the band-gap difference as a function of the short-range fraction of Fock exchange α_s and the inverse screening length μ. Isovalues are shown by solid lines.

These observations have significant consequences for the construction of nonempirical hybrid functionals. In particular, this affects the DD-CAM functionals generated in this work, which include a fraction of Fock exchange $\alpha_s = 1$ in the short range [32]. Therefore it is only meaningful to consider DD-CAM functionals in conjunction with PP2 pseudopotentials. For global hybrid functionals DD-PBE0 and K-PBE0 that

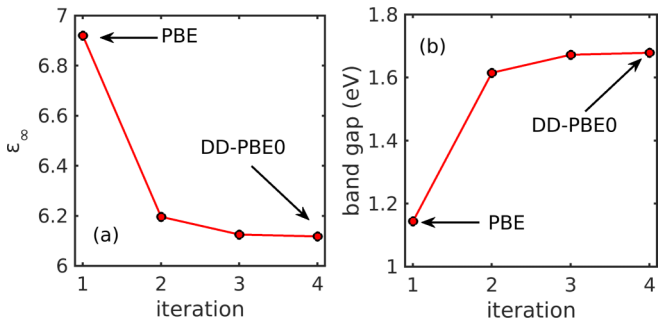

FIG. 4. Convergence of (a) the dielectric constant ε_∞ and (b) the band gap within the self-consistent DD-PBE0 scheme for $CsPbI_3$. The values for the PBE starting point and the converged DD-PBE0 result are highlighted. The present results are obtained with PP1. PP2 pseudopotentials show an analogous behavior.

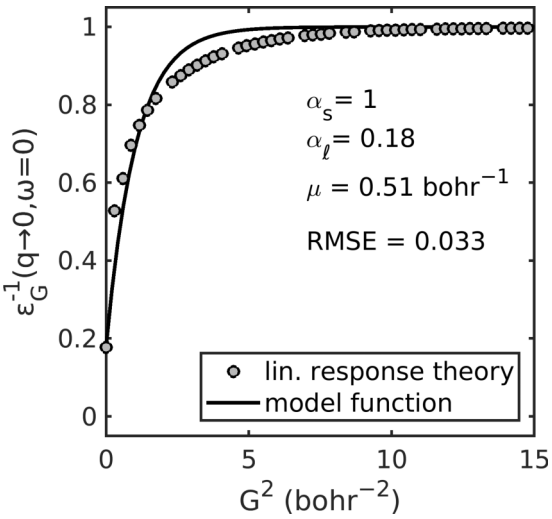

FIG. 5. Inverse dielectric function $\varepsilon_G^{-1}(q \to 0, \omega = 0)$ of $CsPbI_3$ as calculated using linear response theory (circles) and fitted according to the model function (solid line). The fitted values for the functional parameters α_ℓ and μ and for the root-mean-square error (RMSE) are given.

incorporate small fractions of Fock exchange, the implicit treatment of core-electrons leads to smaller deviations and thus the use of the PP1 set entails smaller errors. This should be borne in mind when considering DD-PBE0 and K-PBE0 functionals with PP1 pseudopotentials in Secs. IV A and IV B.

IV. BAND GAPS

A. Dielectric-dependent hybrid functionals

We first focus on the construction of dielectric-dependent hybrid functionals. The convergence of this scheme applied to PBE0(α) functionals is shown in Fig. 4 for the case of $CsPbI_3$. Generally, convergence for the dielectric constant ε_∞ [cf. Fig. 4(a)] and the band gap [cf. Fig. 4(b)] is reached within three to four iterations. The self-consistent update procedure is initialized through the use of the PBE functional, which corresponds to PBE0($\alpha = 0$). We remark that the DD-PBE0 functional resulting from this procedure is independent of the starting point [27].

The band gaps obtained with the DD-PBE0 functional for the present set of perovskites are shown in Table IV and compared to the QS$G\tilde{W}$ reference values. The corresponding mixing parameters α are given in parentheses. On average, we find a band-gap underestimation of ∼0.4 and ∼0.3 eV for PP1 and PP2, respectively. Such an accuracy is comparable to DD-PBE0 results reported in the literature for extended sets of semiconductors and insulators [27,32]. This provides confidence that dielectric-dependent hybrid functionals can achieve the same level of accuracy for a larger set of perovskite materials. The determined mixing parameters are almost identical for both sets of pseudopotentials. This indicates that the explicit treatment of semicore electrons only marginally affects the iterative construction scheme, even though the ensuing band gaps differ by ∼0.1 eV.

TABLE IV. Band gaps (in eV) calculated through DD-PBE0 and DD-CAM functionals. The determined hybrid functional parameter (α) and (α_ℓ, μ) are given in parentheses. The considered set of pseudopotentials is indicated. Band gaps evaluated through QS$G\tilde{W}$ are given as reference. The mean absolute difference (MAD) is given with respect to these values.

	DD-PBE0		DD-CAM	QS$G\tilde{W}$
	PP1	PP2	PP2	PP2
$CsPbI_3$	1.68 (0.16)	1.83 (0.17)	1.99 (0.18, 0.51)	2.27
$CsPbBr_3$	2.48 (0.23)	2.65 (0.23)	2.84 (0.24, 0.53)	3.01
$CsPbCl_3$	3.24 (0.27)	3.32 (0.27)	3.40 (0.28, 0.56)	3.41
$CsSnI_3$	0.60 (0.10)	0.65 (0.10)	0.78 (0.12, 0.48)	1.10
$CsSnBr_3$	0.82 (0.13)	0.88 (0.13)	0.99 (0.15, 0.53)	1.32
$CsSnCl_3$	1.63 (0.21)	1.64 (0.21)	1.75 (0.22, 0.58)	1.79
$CsGeI_3$	1.09 (0.12)	1.17 (0.12)	1.40 (0.10, 0.55)	1.67
$CsGeBr_3$	1.59 (0.17)	1.66 (0.17)	1.89 (0.15, 0.58)	2.13
$CsGeCl_3$	2.44 (0.22)	2.48 (0.22)	2.51 (0.21, 0.60)	2.67
MAD	**0.42**	**0.35**	**0.20**	

Next, we apply the dielectric-dependent approach also to range-separated hybrid functionals. We consider the CAM-type functional, which includes a fraction of Fock exchange α_s in the short range and α_ℓ in the long range, mediated by an inverse screening length μ. The model function given in Eq. (1) enables an accurate description of the inverse dielectric function obtained from linear response theory, as can be seen in Fig. 5 for the case of $CsPbI_3$.

The hybrid functional parameters of the constructed DD-CAM functionals together with the obtained band-gap estimates are given in Table IV. The observed long-range fraction of Fock exchange α_ℓ is in close agreement with the global fraction α found for the DD-PBE0 functionals. This indicates that the long-range exchange interaction is screened with almost identical high-frequency dielectric constants ε_∞ in the two approaches. Consequently, differences in the observed electronic structure originate from the different short-range description. The calculated band gaps indicate a mean absolute difference (MAD) of 0.20 eV with respect to the QS$G\tilde{W}$ reference, which corresponds to an improved description relative to DD-PBE0. Hence, in the dielectric-dependent construction scheme, the range-separated CAM functional yields

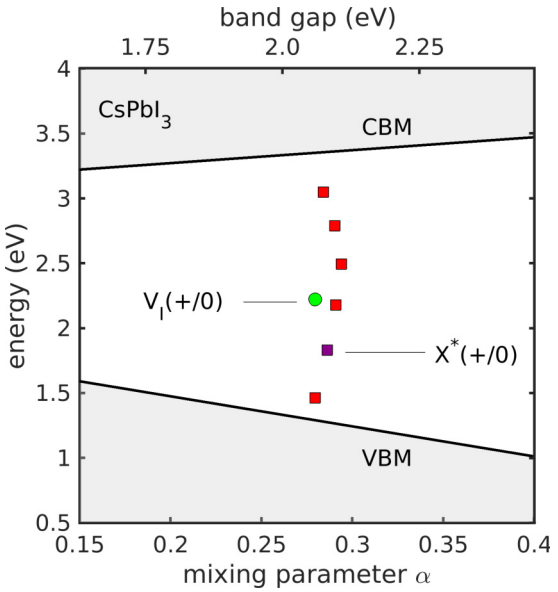

FIG. 6. Band edges and defect energies displayed versus the mixing parameter α for the iodine vacancy V_I (green circle) and various local potential probes (red squares) in $CsPbI_3$. X^* refers to the potential probe with the smallest degree of hybridization with the band edges. The indicated band gaps are obtained with the functional PBE0(α).

more accurate band gaps than the global PBE0 functional, in accord with the results in Ref. [32].

B. Hybrid functionals satisfying Koopmans' condition

We first apply Koopmans' condition to determine the free parameter α within the PBE0(α) functional. We consider various native defects, such as vacancies, interstitials, and antisites, but decide to focus only on halide vacancies since their single-particle energy levels are found to lie close to mid-gap. Indeed, the present construction scheme works most effectively when the hybridization of the defect states with the delocalized band states is minimized [39]. We remark that in our scheme the defect levels are obtained without structural relaxation [36,39], thereby explaining their different location in the band gap with respect to previous studies of defects in such perovskite materials [69–71]. The defect calculations in this section are carried out with the pseudopotential set PP1 due to the computational cost entailed by the consideration of supercells.

To support the choice of the halide-vacancy defect, we use the concept of adjustable hydrogenic-like potential probes [39]. We use potentials resulting from a Gaussian distribution of positive charge with width parameters σ ranging from 0.625 to 1.25 bohr. This allows us to continuously vary the defect level of the localized state across the entire band gap of the host material, as shown in Fig. 6. We observe that the mixing parameter satisfying Koopmans' condition is 0.29 ± 0.01 irrespective of the considered defect. The uncertainty in the mixing parameter results from limitations of the construction scheme [36,39], but yields in this case negligible band-gap deviations of ± 0.02 eV. We identify the optimal potential probe X^* by minimizing the degree of hybridization with the band edges, as described in Ref. [39]. The corresponding band-gap estimate is very close to that obtained with the halide vacancy (cf. Fig. 6). On the basis of this agreement, we focus in the following only on the halide vacancy to construct hybrid functionals satisfying Koopmans' condition.

TABLE V. Band gaps (in eV) calculated through K-PBE0 functionals. The corresponding mixing parameters are given in parentheses. The considered set of pseudopotentials is indicated. Band gaps evaluated through QS$G\tilde{W}$ are given as reference. The mean absolute difference (MAD) is given with respect to these values.

	K-PBE0		QS$G\tilde{W}$
	PP1	PP2	PP2
$CsPbI_3$	2.06 (0.28)	2.28	2.27
$CsPbBr_3$	2.99 (0.35)	3.24	3.01
$CsPbCl_3$	3.87 (0.41)	4.00	3.41
$CsSnI_3$	1.02 (0.23)	1.12	1.10
$CsSnBr_3$	1.34 (0.26)	1.42	1.32
$CsSnCl_3$	2.31 (0.35)	2.29	1.79
$CsGeI_3$	1.46 (0.21)	1.55	1.67
$CsGeBr_3$	2.03 (0.26)	2.12	2.13
$CsGeCl_3$	2.91 (0.32)	2.93	2.67
MAD	**0.21**	**0.20**	

In Table V, the band gaps resulting from the constructed K-PBE0 functionals are reported and compared with QS$G\tilde{W}$ references. We find a MAD of 0.21 eV between the K-PBE0 band gaps and the *GW* references. We remark that the chlorine compounds show larger errors but this effect cannot trivially be related to the electronegativity or to the size of the involved ions. While the origin of these deviations is unclear at the moment, the MAD on the full set of considered compounds is consistent with values in the literature [36]. This consistency supports that this level of accuracy can be expected when considering a larger set of perovskite materials.

It is also of interest to compare the present results with those obtained with DD-PBE0 functionals (cf. Table IV), which share the same functional form of PBE0(α). The mixing parameters of the DD-PBE0 functionals are systematically lower than those of K-PBE0, and so are the corresponding estimates for the band gap. With respect to the *GW* references, the performance of K-PBE0 (MAD = 0.21 eV) is significantly better than that of DD-PBE0 (MAD = 0.42 eV). Hence, for the global functional PBE0(α), the fraction of Fock exchange solely determined through ε_∞ generally leads to underestimated band gaps, while the enforcement of Koopmans' condition yields better results on average. These differences suggest that the physical properties considered in the two construction schemes are not equivalent and that they could potentially be exploited in a complementary fashion. However, the generality of this observation remains to be demonstrated for a larger variety of materials.

Part of the differences between the band gaps obtained with K-PBE0 and QS$G\tilde{W}$ might result from the use of different pseudopotential sets in the two calculations. To evaluate this effect, we determine the band gaps with the PP2 set using the same mixing parameters as obtained from the PP1 defect calculations. We hereby rely on the fact that the

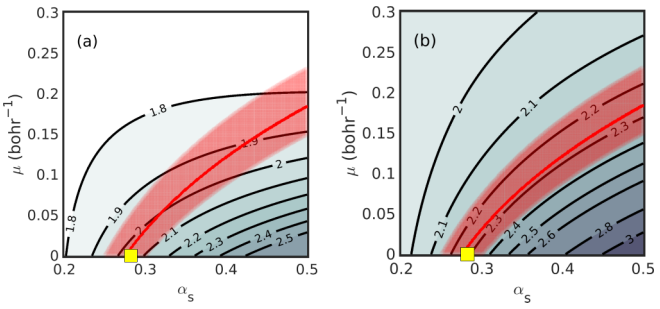

FIG. 7. Isocontour plots for K-CAM band gaps of $CsPbI_3$ as a function of the short-range fraction of Fock exchange α_s and the inverse screening length μ. The parameter α_ℓ is fixed to $1/\varepsilon_\infty$. The displayed band gaps are obtained with (a) PP1 and (b) PP2 pseudopotentials. The red lines indicate the fulfillment of Koopmans condition, and the regions shaded in red deviations below 0.1 eV. The point in parameter space corresponding to the K-PBE0 functional is highlighted with a yellow square.

mixing parameters remain almost unchanged upon varying the pseudopotential set, as seen in Table IV for DD-PBE0. Table V shows that this generally yields an increase of the resulting band gaps as a consequence of the trend in Fig. 3. However, the overall accuracy (MAD = 0.20 eV) remains similar to that achieved with PP1 (MAD = 0.21 eV) and thus the considerations made above remain unaffected.

Next, it is our interest to study the accuracy of CAM hybrid functionals when enforcing Koopmans' condition. As discussed in Sec. III B, such calculations require the explicit treatment of semicore electrons, i.e., the use of the demanding PP2 pseudopotentials. To circumvent this problem, we determine the free parameters of the CAM functional by performing defect supercell calculations with PP1 pseudopotentials. We then obtain band-gap estimates from bulk calculations of the primitive unit cell using the constructed CAM functional with either PP1 or PP2 pseudopotentials.

We illustrate this procedure for the iodine vacancy V_I in $CsPbI_3$ in Fig. 7. In the investigated CAM functionals, α_ℓ is fixed to $1/\varepsilon_\infty$, while α_s and μ are varied systematically. We only consider $\alpha_s < 0.5$ due to the decreasing reliability of the PP1 pseudopotentials with increasing α_s (cf. Fig. 3). The parameters fulfilling Koopmans' condition are identified by the red curve within the two-dimensional (α_s, μ) space. In Ref. [36], it was found that such lines remain close to band-gap isolines, thereby providing a robust determination of the band gap irrespective of the location on the curve fulfilling Koopmans' condition (Koopmans' curve). This behavior is not seen for PP1 pseudopotentials [Fig. 7(a)], but is recovered when the PP2 set is used [Fig. 7(b)]. In the latter case, the band gap always remains close to ∼2.3 eV, in agreement with the band gap achieved with the global functional K-PBE0. These results suggest that the deviation of the Koopmans' curve from a band-gap isoline for PP1 pseudopotentials is a consequence of the discrepancies pointed out in Fig. 3. Nevertheless, the hybrid-functional parameters determined with PP1 pseudopotentials appear to have a more extended range of validity than the band-gap values, in a similar way as seen above for DD-PBE0 functionals (cf. Table IV). Overall, to close this section on the use of Koopmans' condition for determining the parameters, we conclude that the K-CAM functional does not bring any improvement over the K-PBE0 functional. This is in agreement with the findings of Ref. [36].

V. CONCLUSIONS

In this work, we applied two nonempirical schemes for the construction of hybrid functionals to a set of inorganic metal-halide perovskites. We set out to determine the accuracy by which such nonempirical hybrid functionals are capable of predicting band gaps. For this purpose, we also performed state-of-the-art *GW* calculations, which we used as reference. The free parameters of the hybrid functionals in the first scheme were fixed through the dielectric response, while the enforcement of Koopmans' condition on defect states was the criterion at the basis of the second scheme. Moreover, we investigated two classes of functionals: global functionals with a single undetermined parameter and range-separated CAM-type functionals involving three parameters. In all cases, the parameters to be determined refer to the way Fock exchange is incorporated in the functional.

The dielectric-dependent approach based on global functionals yields a mean average deviation of 0.35 eV with respect to the *GW* references. This deviation is in line with previous results in the literature on other materials [27,32]. The consideration of range-separated functionals reduces the mean average deviation to 0.20 eV, confirming thereby that the use of this type of functional leads to a higher accuracy [30,32]. Global hybrid functionals fulfilling Koopmans' condition also yield band gaps in good agreement with our *GW* references, as indicated by the mean average deviation of 0.20 eV. Consideration of CAM-type functionals supports the robustness of the predicted band gaps [36], and hence does not lead to any further improvement in the accuracy. Overall, the two applied schemes yield band gaps with an accuracy of ∼0.2 eV. For this, the dielectric-dependent scheme requires the use of range-separated functionals, but plain global functionals are sufficient within the scheme based on Koopmans' condition. More generally, the differing features of the two schemes hint at the fact that reproducing the dielectric response and imposing Koopmans' condition are nonequivalent constraints. This might deserve further investigation to benefit from the individual advantages of the two schemes in a combined fashion.

On the practical side, the dielectric-dependent scheme only involves bulk calculations for the primitive unit cell, whereas the scheme based on Koopmans' condition requires the consideration of localized defect states and thus the treatment of supercells of suitable size. The latter condition can imply demanding computational resources and restrict the overall flexibility of the scheme, as seen in the present work as far as the class of pseudopotentials that could be treated. Furthermore, the use of Koopmans' condition necessitates the identification of defect states lying in the middle of the band gap. This is a material-dependent issue which complicates the incorporation of Koopmans' condition in automatized procedures.

In view of applying such nonemperical schemes to a larger class of perovskite materials, we conclude that the dielectric-dependent scheme with range-separated functionals is the most suitable, both for the accuracy achieved and for the computational cost involved. Hence, it stands out as a viable scheme to achieve accurate band gaps in the high-throughput screening of perovskite materials.

ACKNOWLEDGMENTS

We thank Igor Reshetnyak for fruitful discussions on Koopmans' condition. Support from the Swiss National Science Foundation (SNSF) is acknowledged under Grant No. 200020-172524. The calculations have been performed at Swiss National Supercomputing Center (CSCS) and at SCITAS-EPFL.

[1] A. Kojima, K. Teshima, Y. Shirai, and T. Miyasaka, J. Am. Chem. Soc. **131**, 6050 (2009).
[2] J. Burschka, N. Pellet, S.-J. Moon, R. Humphry-Baker, P. Gao, M. K. Nazeeruddin, and M. Grätzel, Nature **499**, 316 (2013).
[3] G. Hodes, Science **342**, 317 (2013).
[4] S. Razza, S. Castro-Hermosa, A. Di Carlo, and T. M. Brown, APL Mater. **4**, 091508 (2016).
[5] W. S. Yang, B.-W. Park, E. H. Jung, N. J. Jeon, Y. C. Kim, D. U. Lee, S. S. Shin, J. Seo, E. K. Kim, J. H. Noh, and S. I. Seok, Science **356**, 1376 (2017).
[6] I. E. Castelli, J. M. García-Lastra, K. S. Thygesen, and K. W. Jacobsen, APL Mater. **2**, 081514 (2014).
[7] M. R. Filip and F. Giustino, J. Phys. Chem. C **120**, 166 (2016).
[8] S. Körbel, M. A. L. Marques, and S. Botti, J. Mater. Chem. C **4**, 3157 (2016).
[9] L. Hedin, Phys. Rev. **139**, A796 (1965).
[10] M. van Schilfgaarde, T. Kotani, and S. Faleev, Phys. Rev. Lett. **96**, 226402 (2006).
[11] M. Shishkin, M. Marsman, and G. Kresse, Phys. Rev. Lett. **99**, 246403 (2007).
[12] W. Chen and A. Pasquarello, Phys. Rev. B **92**, 041115(R) (2015).
[13] J. Wiktor, U. Rothlisberger, and A. Pasquarello, J. Phys. Chem. Lett. **8**, 5507 (2017).
[14] A. D. Becke, J. Chem. Phys. **98**, 1372 (1993).
[15] J. P. Perdew, M. Ernzerhof, and K. Burke, J. Chem. Phys. **105**, 9982 (1996).
[16] J. Heyd, G. E. Scuseria, and M. Ernzerhof, J. Chem. Phys. **118**, 8207 (2003).
[17] T. Yanai, D. P. Tew, and N. C. Handy, Chem. Phys. Lett. **393**, 51 (2004).
[18] A. Alkauskas, P. Broqvist, and A. Pasquarello, Phys. Status Solidi B **248**, 775 (2011).
[19] W. Kohn and L. J. Sham, Phys. Rev. **140**, A1133 (1965).
[20] L. J. Sham and M. Schlüter, Phys. Rev. Lett. **51**, 1888 (1983).
[21] J. P. Perdew, K. Burke, and M. Ernzerhof, Phys. Rev. Lett. **77**, 3865 (1996).
[22] T. Shimazaki and Y. Asai, Chem. Phys. Lett. **466**, 91 (2008).
[23] T. Shimazaki and Y. Asai, J. Chem. Phys. **130**, 164702 (2009).
[24] T. Shimazaki and Y. Asai, J. Chem. Phys. **132**, 224105 (2010).
[25] M. A. L. Marques, J. Vidal, M. J. T. Oliveira, L. Reining, and S. Botti, Phys. Rev. B **83**, 035119 (2011).
[26] S. Refaely-Abramson, S. Sharifzadeh, N. Govind, J. Autschbach, J. B. Neaton, R. Baer, and L. Kronik, Phys. Rev. Lett. **109**, 226405 (2012).
[27] J. H. Skone, M. Govoni, and G. Galli, Phys. Rev. B **89**, 195112 (2014).
[28] M. Gerosa, C. E. Bottani, L. Caramella, G. Onida, C. Di Valentin, and G. Pacchioni, Phys. Rev. B **91**, 155201 (2015).
[29] M. Gerosa, C. Di Valentin, C. E. Bottani, G. Onida, and G. Pacchioni, J. Chem. Phys. **143**, 111103 (2015).
[30] J. H. Skone, M. Govoni, and G. Galli, Phys. Rev. B **93**, 235106 (2016).
[31] M. Gerosa, C. E. Bottani, C. D. Valentin, G. Onida, and G. Pacchioni, J. Phys. Condens. Matter **30**, 044003 (2017).
[32] W. Chen, G. Miceli, G.-M. Rignanese, and A. Pasquarello, Phys. Rev. Mater. **2**, 073803 (2018).
[33] B. Sadigh, P. Erhart, and D. Åberg, Phys. Rev. B **92**, 075202 (2015).
[34] P. Deák, Q. Duy Ho, F. Seemann, B. Aradi, M. Lorke, and T. Frauenheim, Phys. Rev. B **95**, 075208 (2017).
[35] S. Kokott, S. V. Levchenko, P. Rinke, and M. Scheffler, New J. Phys. **20**, 033023 (2018).
[36] G. Miceli, W. Chen, I. Reshetnyak, and A. Pasquarello, Phys. Rev. B **97**, 121112(R) (2018).
[37] T. J. Smart, F. Wu, M. Govoni, and Y. Ping, Phys. Rev. Mater. **2**, 124002 (2018).
[38] A. R. Elmaslmane, M. B. Watkins, and K. P. McKenna, J. Chem. Theory Comp. **14**, 3740 (2018).
[39] T. Bischoff, I. Reshetnyak, and A. Pasquarello, Phys. Rev. B **99**, 201114(R) (2019).
[40] P. Deák, M. Lorke, B. Aradi, and T. Frauenheim, J. Appl. Phys. **126**, 130901 (2019).
[41] A. Seidl, A. Görling, P. Vogl, J. A. Majewski, and M. Levy, Phys. Rev. B **53**, 3764 (1996).
[42] J. P. Perdew, R. G. Parr, M. Levy, and J. L. Balduz, Phys. Rev. Lett. **49**, 1691 (1982).
[43] P. Mori-Sánchez, A. J. Cohen, and W. Yang, J. Chem. Phys. **125**, 201102 (2006).
[44] P. Mori-Sánchez, A. J. Cohen, and W. Yang, Phys. Rev. Lett. **100**, 146401 (2008).
[45] Z. H. Levine and D. C. Allan, Phys. Rev. Lett. **63**, 1719 (1989).
[46] C. Friedrich, M. C. Müller, and S. Blügel, Phys. Rev. B **83**, 081101(R) (2011).
[47] S. Lebègue, B. Arnaud, M. Alouani, and P. E. Bloechl, Phys. Rev. B **67**, 155208 (2003).
[48] X. Gonze, B. Amadon, P.-M. Anglade, J.-M. Beuken, F. Bottin, P. Boulanger, F. Bruneval, D. Caliste, R. Caracas, M. Côté *et al.*, Comp. Phys. Commun. **180**, 2582 (2009).
[49] C. C. Stoumpos, C. D. Malliakas, and M. G. Kanatzidis, Inorg. Chem. **52**, 9019 (2013).
[50] G. E. Eperon, S. D. Stranks, C. Menelaou, M. B. Johnston, L. M. Herz, and H. J. Snaith, Energy Environ. Sci. **7**, 982 (2014).
[51] M. Sebastian, J. A. Peters, C. C. Stoumpos, J. Im, S. S. Kostina, Z. Liu, M. G. Kanatzidis, A. J. Freeman, and B. W. Wessels, Phys. Rev. B **92**, 235210 (2015).

[52] J. B. Hoffman, A. L. Schleper, and P. V. Kamat, J. Am. Chem. Soc. **138**, 8603 (2016).
[53] L. Peedikakkandy and P. Bhargava, RSC Adv. **6**, 19857 (2016).
[54] I. Chung, J.-H. Song, J. Im, J. Androulakis, C. D. Malliakas, H. Li, A. J. Freeman, J. T. Kenney, and M. G. Kanatzidis, J. Am. Chem. Soc. **134**, 8579 (2012).
[55] C. C. Stoumpos, L. Frazer, D. J. Clark, Y. S. Kim, S. H. Rhim, A. J. Freeman, J. B. Ketterson, J. I. Jang, and M. G. Kanatzidis, J. Am. Chem. Soc. **137**, 6804 (2015).
[56] T. Krishnamoorthy, H. Ding, C. Yan, W. L. Leong, T. Baikie, Z. Zhang, M. Sherburne, S. Li, M. Asta, N. Mathews, and S. G. Mhaisalkar, J. Mater. Chem. A **3**, 23829 (2015).
[57] Z.-G. Lin, L.-C. Tang, and C.-P. Chou, Opt. Mater. **31**, 28 (2008).
[58] G. Thiele, H. W. Rotter, and K. D. Schmidt, Z. Anorg. allg. Chem. **545**, 148 (1987).
[59] D. R. Hamann, Phys. Rev. B **88**, 085117 (2013).
[60] M. van Setten, M. Giantomassi, E. Bousquet, M. Verstraete, D. Hamann, X. Gonze, and G.-M. Rignanese, Comput. Phys. Commun. **226**, 39 (2018).
[61] A. Stroppa and G. Kresse, New J. Phys. **10**, 063020 (2008).
[62] F. Gygi and A. Baldereschi, Phys. Rev. B **34**, 4405 (1986).
[63] W. Chen and A. Pasquarello, Phys. Rev. B **90**, 165133 (2014).
[64] S. L. Adler, Phys. Rev. **126**, 413 (1962).
[65] N. Wiser, Phys. Rev. **129**, 62 (1963).
[66] S. Sharma, J. K. Dewhurst, A. Sanna, and E. K. U. Gross, Phys. Rev. Lett. **107**, 186401 (2011).
[67] W. Chen and A. Pasquarello, J. Phys. Condens. Matter **27**, 133202 (2015).
[68] P. Giannozzi, S. Baroni, N. Bonini, M. Calandra, R. Car, C. Cavazzoni, D. Ceresoli, G. L. Chiarotti, M. Cococcioni, I. Dabo *et al.*, J. Phys. Condens. Matter **21**, 395502 (2009).
[69] M.-H. Du, J. Phys. Chem. Lett. **6**, 1461 (2015).
[70] J. Kang and L.-W. Wang, J. Phys. Chem. Lett. **8**, 489 (2017).
[71] J. Wiktor, F. Ambrosio, and A. Pasquarello, J. Mater. Chem. A **6**, 16863 (2018).